
Article:

Cizauskas, M., Kors, A., Reithmaier, J.P. et al. (2026) Layer-dependent spin properties of charge carriers in vertically coupled telecom quantum dots. Physical Review B, 113 (3). 035441. ISSN: 2469-9950

https://doi.org/10.1103/xmz7-18rg

PHYSICAL REVIEW B **113**, 035441 (2026)

Layer-dependent spin properties of charge carriers in vertically coupled telecom quantum dots

Marius Cizauskas,[1,2,*] A. Kors,[3] J. P. Reithmaier,[3] A. Mark Fox,[2] M. Benyoucef,[3,†]
Manfred Bayer,[1] and Alex Greilich[1,‡]
[1]*Experimentelle Physik 2, Technische Universität Dortmund, 44221 Dortmund, Germany*
[2]*Department of Physics and Astronomy, University of Sheffield, Sheffield, United Kingdom*
[3]*Institute of Nanostructure Technologies and Analytics (INA), CINSaT, University of Kassel, D-34132 Kassel, Germany*

(Received 18 September 2025; revised 18 November 2025; accepted 9 January 2026; published 28 January 2026)

We investigate the spin properties of charge carriers in vertically coupled InAs/InAlGaAs quantum dots grown by molecular beam epitaxy, emitting at telecom C-band wavelengths, with a silicon δ-doped layer. Using time-resolved pump-probe Faraday ellipticity measurements, we systematically study single-, two-, and four-layer quantum dot (QD) configurations to quantify how vertical coupling affects key spin-coherence parameters. Our measurements reveal distinct layer-dependent effects: (i) Adding a second QD layer flips the resident charge from electrons to holes, consistent with optically induced electron tunneling into lower-energy dots and resultant hole charging. (ii) Starting from the four-layer sample, the pump-probe signal develops an additional nonoscillating, decaying component absent in single- and two-layer samples, attributed to multiple layer growth changing the strain environment, which reduces heavy-hole and light-hole mixing. (iii) With four layers or more, hole spin mode locking (SML) can be observed, enabling quantitative extraction of the hole coherence time $T_2 \approx 13$ ns from SML amplitude saturation. We also extract longitudinal spin relaxation (T_1) and transverse (T_2^*) spin dephasing times, g-factors, and inhomogeneous dephasing parameters for both electrons and holes across all layer configurations. The hole spin dephasing times T_2^* remain relatively constant (2.3–2.7 ns) across layer counts, while longitudinal relaxation times T_1 decrease with increasing layers (from 0.9 μs for single-layer to 0.32 μs for four-layer samples). These findings provide potential design guidelines for engineering spin coherence in telecom-band QDs for quantum information applications.

DOI: 10.1103/xmz7-18rg

I. INTRODUCTION

The advancement of quantum information and communication technologies relies on the development of high-quality quantum systems that can maintain coherence over extended timescales while operating under practical conditions. Semiconductor quantum dots (QDs) have emerged as versatile platforms for quantum information applications due to their potential for optical control of spin states, scalable fabrication, the possibility of on-chip integration, and use as high-purity single-photon sources [1–3].

For quantum information applications, operation at telecom wavelengths (1.3–1.6 μm) offers practical advantages, namely the possibility to use existing telecom fiber infrastructure. Efficient QD coupling to single-mode fiber has been demonstrated with additional nanostructures designed to reduce losses [4,5]. InAs/InGaAs/InP QDs are a promising solution for telecom-band quantum information applications, as they can be engineered to emit efficiently in the C-band while maintaining the spin coherence properties necessary for quantum applications [6,7].

The ultimate performance of QD spin-based quantum information systems is governed by the coherence properties of the carrier spins, which are subject to decoherence from hyperfine interactions, phonon scattering, and structural asymmetries [6,8]. Molecular beam epitaxy (MBE) has been the predominant growth technique for high-quality QDs, offering precise control over layer thickness, composition, and doping profiles [9]. However, the specific growth conditions and structural parameters can significantly influence the resulting spin coherence properties.

An important consideration in QD design is the impact of layer structure on spin dynamics. While single-layer QD structures offer simplicity, multilayer configurations can provide enhanced optical signals and the potential for engineering interlayer interactions [10–12]. The samples investigated in this work are InAs/InAlGaAs QDs grown by MBE, with a structure identical to that reported by Ref. [7], with the difference that in Ref. [7] the sample consists of eight layers. We focus on comparing the spin properties of single-, two-, and four-layer stacks of QD configurations to quantify how additional layers affect key spin-coherence parameters. Using time-resolved pump-probe Faraday ellipticity, we extract longitudinal and transverse relaxation times, *g*-factors, and inhomogeneous dephasing for electrons and holes.

---

[*] Contact author: marius.cizauskas@tu-dortmund.de

[†] Contact author: m.benyoucef@physik.uni-kassel.de

[‡] Contact author: alex.greilich@tu-dortmund.de

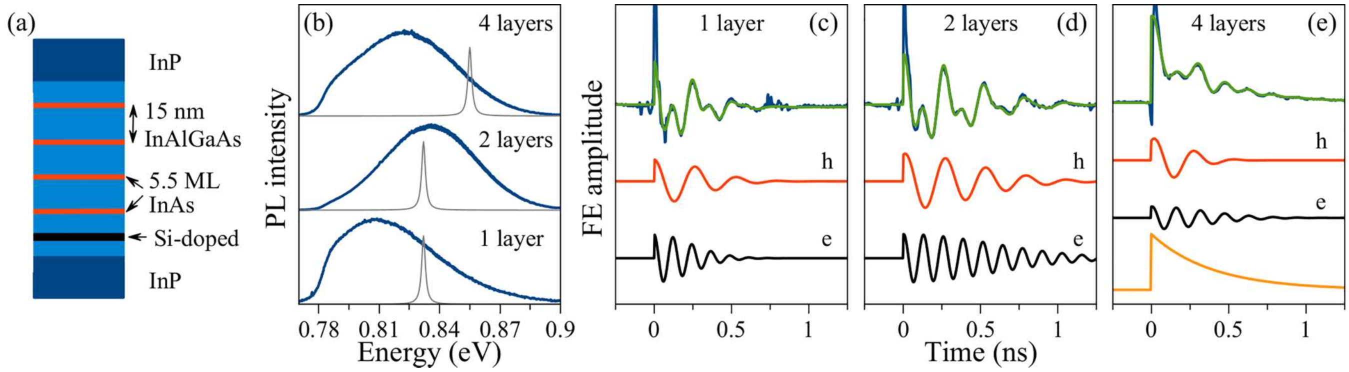

FIG. 1. (a) Example of a four-layer InAs/InAlGaAs stacked QD sample structure. Photoluminescence (PL) spectra and Faraday ellipticity measurements for QD samples with varying numbers of layers are presented in the subsequent plots. Panel (b) shows PL intensity spectra (offset for clarity), with the laser excitation spectrum shown as a gray line for each sample. All PL spectra were obtained with a 2.33 eV laser as the excitation source. For Faraday ellipticity, 0.832 eV excitation was used for the single- and two-layer samples, and 0.855 eV for the four-layer sample. Panels (c), (d), and (e) show time-resolved Faraday ellipticity amplitude measurements in blue color for the one-layer, two-layer, and four-layer samples, respectively, with green color fitting using Eq. (9). The colored traces below show the fit decomposition, with red traces corresponding to hole spin precession, black traces to electron spin precession, and the orange trace [in panel (e)] representing an additional exponential decay component that may arise from interdot coupling or other multidot interactions. The component measurements were all done at a transverse magnetic field strength of 0.4 T. The pump and probe powers for the single-layer sample were 15 and 2 mW, for the two-layer sample they were 20 and 2 mW, and for the four-layer sample they were 10 and 2 mW. All measurements were done at 6 K.

Across otherwise-identical stacks, we uncover clear layer-dependent trends. First, adding a second QD layer flips the effective optically induced doping from electrons to holes, consistent with optically induced electron tunneling into lower-energy dots and resultant hole charging. Second, in four-layer stacks, the pump-probe signal exhibits an additional nonoscillatory decay component absent in one- and two-layer samples, which we attribute to potential interlayer coupling that modifies the valence-band structure and reduces heavy-hole–light-hole (HH-LH) mixing. Finally, the four-layer sample supports hole spin mode locking (SML), enabling the quantitative extraction of the hole coherence time $T_2 \approx 13$ ns from SML amplitude saturation.

This layer-resolved study identifies how vertical coupling reshapes spin properties in telecom-band QDs and provides design guidelines for engineered coherence. Since multiple-layer structures shift to holes as the primary charge carriers, coherence remains robust due to the weak hyperfine coupling of holes. In this paper, we present measurements and results that provide a systematic assessment of layer-dependent spin behavior, essential for determining how multilayer QD structures can be used constructively in telecom-wavelength spin-photon platforms.

II. EXPERIMENTAL DETAILS

The QD samples investigated in this study are fabricated using MBE Stranski-Krastanov (SK) growth method on (100)-oriented InP substrates. The samples contain InAs QDs embedded within $In_{0.53}Al_{0.24}Ga_{0.23}As$ barrier layers, following the same structural design and growth parameters as reported by Ref. [7], see Fig. 1(a). The only difference between our samples is the number of layers.

Each InAs layer consists of 5.5 monolayers (equivalent to approximately 1.65 nm) with QDs having a surface density of approximately $10^{10}\,\mathrm{cm}^{-2}$. A silicon δ-doped layer is positioned 15 nm below the QD layers with a doping concentration of $10^{10}\,\mathrm{cm}^{-2}$ to provide resident electrons within the QDs. In the two-layer sample, the QD layers are separated by 15 nm of $In_{0.53}Al_{0.24}Ga_{0.23}As$ barrier material. The quaternary barrier composition serves the dual purpose of providing enhanced carrier confinement.

Optical measurements are conducted using a liquid helium bath cryostat equipped with temperature control capabilities, allowing measurements across a temperature range from 6 to 60 K. Magnetic field application is achieved through a superconducting magnet system capable of providing fields up to 4 T. The magnetic field orientation can be configured either parallel to the optical excitation axis (Faraday configuration) or perpendicular to it (Voigt configuration) by mechanical rotation of the sample mount and cryostat.

The optical excitation source consists of a mode-locked Ti:sapphire laser (MiraHP) operating at a repetition frequency of 76.7 MHz, which pumps an optical parametric oscillator (APE OPO) to generate tunable pulses in the telecom wavelength range. The laser output provides pulses with approximately 2 nm spectral bandwidth. The generated beam is divided into pump and probe paths using a beam splitter, with the probe beam directed through a computer-controlled mechanical delay stage for temporal scanning.

Both pump and probe beams are focused onto the sample surface, with the pump beam diameter set to 150 μm and the probe beam focused to 100 μm diameter to ensure complete spatial overlap. The excitation energy is tuned to coincide with the photoluminescence peak at approximately 0.83 eV to achieve resonant excitation of the QD ensemble.

Spin polarization in the QDs is generated using circularly polarized pump pulses, achieved through an electro-optic modulator that alternates the pump polarization between σ^+ and σ^- states at frequencies ranging from 1 kHz to 2 MHz (with 10 kHz used for Voigt geometry measurements). The probe beam is linearly polarized, and the intensity is modulated using a photoelastic modulator operating at 86 kHz, followed by a Glan-Thompson polarizer.

Spin-dependent optical rotation of the probe beam is detected through Faraday ellipticity measurements [13]. Following interaction with the sample, the probe beam passed through a 10 μm diameter pinhole to minimize detection of scattered pump light. A quarter-wave plate converts the circular components of an elliptically polarized probe into linearly polarized components with orthogonal orientations. These components are separated using a Wollaston prism and directed onto balanced photodiodes for differential detection.

The photodiode signals are processed using lock-in amplification at the difference frequency between the pump and probe modulation frequencies, providing an enhanced signal-to-noise ratio and rejection of common-mode noise sources. This double-modulation detection scheme enables measurement of small spin-induced optical rotations with high sensitivity.

III. EXPERIMENTAL RESULTS

Figure 1(b) shows the photoluminescence (PL) spectra of all the samples (blue curves; gray curves show excitation). The PL comparison of the different samples shows consistency; most of the change is observed where the sample is excited. The pump-probe excitation energy was determined by optimizing the tradeoff between signal amplitude and experimental noise. The wavelength selection accounted not only for the excitation efficiency but also for wavelength-dependent laser stability and sample inhomogeneities. We selected the excitation energies that yielded the highest effective signal-to-noise ratio, ensuring robust fitting for both electron and hole precession signals. For the one- and four-layer samples, the results are consistent and can be explained by the fact that at higher energies, more dots are excited, leading to higher signal amplitude. In the four-layer sample, the excitation is shifted to higher energies to obtain a higher amplitude for the hole spin component due to the spin mode-locking effect discussed later in the paper. In a two-layer sample, the excitation is placed at a lower energy than the PL center to obtain a robust signal.

When a transverse magnetic field is applied in the Voigt direction, the samples exhibit characteristic oscillatory Faraday ellipticity signals [blue curve and the signal fit in green in panels (c)–(e) of Fig. 1], as shown in Figs. 1(c)–1(e) for a field of 0.4 T. These oscillations arise from the Larmor precession of electron (black curve) and hole (red curve) spins, with each carrier type contributing a distinct frequency component. The signals can be fitted and decomposed using

$$S = \sum_i A_i \cos(\omega_i t) \exp\left(-\frac{t^2}{2T_{2,i}^{*2}}\right), \tag{1}$$

where i denotes the carrier type (electron or hole), A_i is the amplitude, ω_i is the Larmor precession frequency, and $T_{2,i}^*$ is the spin dephasing time. The Larmor frequency is related to the applied magnetic field through

$$\omega_i = \frac{g_i \mu_B B_V}{\hbar}, \tag{2}$$

where g_i is the g-factor of the respective carrier, μ_B is the Bohr magneton, B_V is the transverse magnetic field strength, and $\hbar$ is the reduced Planck constant. Holes have a higher effective mass than electrons, leading to more localized wave functions and correspondingly smaller g-factors, which results in lower precession frequencies [14,15].

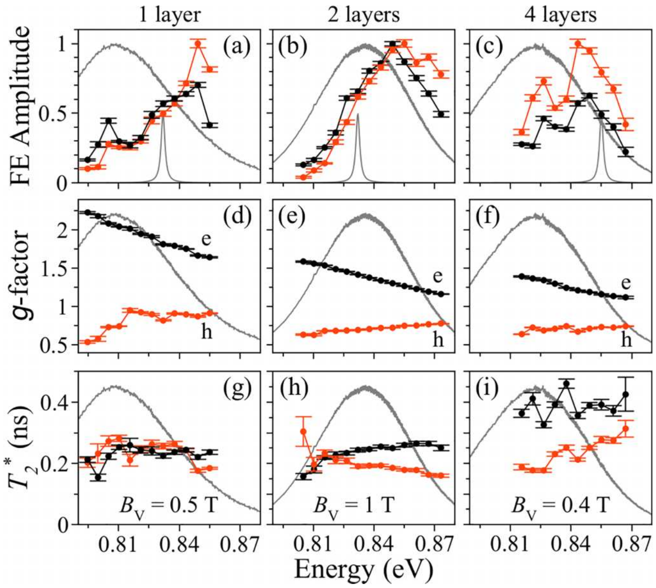

FIG. 2. Energy-dependent parameter characterization for QD samples with different numbers of layers (one, two, and four layers). Panels (a), (b), and (c) display the normalized Faraday ellipticity amplitudes A_i from Eq. (9), red points represent holes, and black ones electrons. Gray lines additionally show the PL and the laser pulse profile for later experiments. Panels (d), (e), and (f) show the extracted Lande g-factors. Panels (g), (h), and (i) show the spin dephasing times $T_{2,i}^*$ measured at magnetic field values shown in the panels. Pump powers for the one-layer sample were 15 mW, and for two- and four-layer samples, 20 mW. All measurements were performed at 6 K and a probe power of 2 mW.

A further result can be observed in Fig. 1(e), where, alongside the electron and hole precessions, there is an additional nonoscillating exponential decay element [orange curve in panel (e)], which is also observed in the eight-layer sample investigated in Ref. [7]. One possible explanation is the presence of a tilted magnetic field component, which provides an additional Faraday geometry component that causes the exponential decay. However, with further anisotropy measurements and the fact that this phenomenon is not observed in samples with two or one layers, we demonstrate that it is most probably related to interlayer dot coupling and varying strain environment between the QD layers, which can affect heavy-hole and light-hole mixing.

Figure 2 shows the change of sample properties with varied excitation energy. The columns correspond to one-, two-, and four-layer structures, respectively, and the rows correspond to Faraday ellipticity, g-factor, and spin dephasing measurements, respectively. The black data points correspond to electrons and red to holes. In gray, the PL is shown, and in panels (a), (b), and (c), the excitation spectra is displayed. The Faraday ellipticity measurements show the expected results: the highest amplitude at higher energies after the PL peak. The excitation is placed to account for both the Faraday ellipticity amplitude and the signal-to-noise ratio, which is why

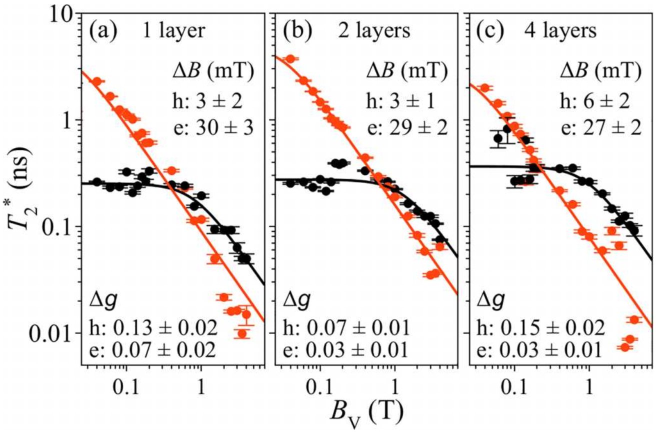

FIG. 3. Spin dephasing time (T_2^*) measurements as a function of transverse magnetic field (B_V) for InAs/InAlGaAs QD samples with different numbers of layers. The data are presented on log-log scales for samples containing one, two, and four QD layers [panels (a), (b), and (c), respectively]. Red circles represent hole spin dephasing times, and black circles represent electron spin dephasing times. The solid lines show fits to the experimental data using a model that accounts for g-factor spread and magnetic field fluctuations. The fitting parameters, including magnetic field spreads (ΔB_h, ΔB_e) and g-factor spreads (Δg_h, Δg_e), are displayed for each sample. The measurement configuration is the same as in Fig. 1.

the excitation energy is offset from the amplitude maxima. The g-factor dependency shows the absolute electron g-factor decreasing and increasing for holes, which is in line with what is observed in similar telecom QD samples [7,16,17] and agrees with the Roth-Lax-Zwerdling relation for bulk semiconductors [18]. The spin dephasing measurements do not show any significant trends with changing excitation energy. It should be noted that all data displayed here are with error bars. However, in some cases, the error is small, so the error bars are not clearly visible.

The spin dephasing times (red data points correspond to holes and black to electrons), displayed in Figs. 3(a)–3(c) for single-, two-, and four-layer structures, respectively, show a characteristic dependence on the applied transverse magnetic field strength. At low magnetic fields, dephasing is dominated by hyperfine interactions with nuclear spins. In contrast, at higher fields, inhomogeneities in the QD ensemble, which cause a spread in the g-factor, become the limiting factor. This behavior is described by [7]

$$T_{2,i}^* = \frac{\hbar}{\sqrt{(\Delta g_i \mu_B B_V)^2 + (g_i \mu_B \Delta B_i)^2}}, \tag{3}$$

where Δg_i represents the g-factor spread due to variations in QD size and composition, and ΔB_i characterizes the magnetic field fluctuations resulting from hyperfine interactions.

From the fits to the dephasing equation in Eq. (3), we extract significantly different g-factor spreads for the three samples, shown in Table I. The single-layer sample shows the largest g-factor spreads for both electrons and holes, along with considerable magnetic field fluctuation spreads. The two-layer sample exhibits reduced g-factor spreads for both carrier types, while magnetic-field fluctuation spreads remain similar. The four-layer sample demonstrates a similar electron g-factor spread compared to the two-layer sample, but shows a significant increase in hole g-factor spread, while magnetic field fluctuation spreads remain comparable to the previous samples. The magnetic field fluctuations, which reflect the strength of hyperfine interactions, show some variation between samples but stay in the same order of magnitude, suggesting similar nuclear spin environments in all three structures. There is a more significant difference between our three samples and the eight-layer sample in Ref. [7] in terms of magnetic field fluctuation values ΔB_i. This substantial deviation of the electron field fluctuation component might be related to the weaker localization of the tunneling electrons.

The g-factor spread shows more significant variation compared to the magnetic field spread. The reduced g-factor spread in the two-layer sample may indicate improved structural uniformity or different growth dynamics compared to the single-layer sample; however, the more likely explanation is that the excitation energy remains the same while the PL of the two-layer sample blue-shifts. This results in the effective excited PL width being significantly smaller than in the single-layer sample, indicating that the size distribution of the excited QDs is narrower than in the single-layer case, leading to a smaller g-factor spread. Another contributing factor is that due to the PL blue shift, higher-energy QDs are excited. It has been demonstrated that higher-energy transitions tend to have lower g-factor spreads [19], which is consistent with our reduced g-factor spread. A similar argument applies to the four-layer sample, where the PL is redshifted and the excitation energy is higher than in the other two samples, thereby increasing the hole g-factor spread. It is of interest to note that in both cases, the electron g-factor spread is smaller than that of the hole, and even decreases relative to the hole g-factor spread in the two-layer and four-layer structures. Compared to Ref. [7], it would be expected that the electron g-factor spread would become larger than for holes with an increasing layer amount. This is further addressed in the Sec. IV.

Lastly, the obtained transverse g-factors for the different samples are shown in Table I. There is minimal change in the

TABLE I. Different sample g-factor values, g-factor spreads, and magnetic field fluctuation spreads extracted from dephasing Eqs. (9) and (3) fits for electron and hole carriers across four QD layer structures.

Sample type	$\lvert g_e \rvert$	$\lvert g_h \rvert$	Δg_e	Δg_h	ΔB_e (mT)	ΔB_h (mT)
Single-layer	1.51 ± 0.01	0.64 ± 0.01	0.07 ± 0.02	0.13 ± 0.02	30 ± 3	3 ± 2
Two-layers	1.42 ± 0.01	0.72 ± 0.01	0.03 ± 0.01	0.07 ± 0.01	29 ± 2	3 ± 1
Four-layers	1.15 ± 0.01	0.49 ± 0.01	0.03 ± 0.01	0.15 ± 0.02	27 ± 2	6 ± 2
Eight-layers [7]	1.88 ± 0.02	0.60 ± 0.01	0.15 ± 0.03	0.09 ± 0.01	14 ± 2	8 ± 2

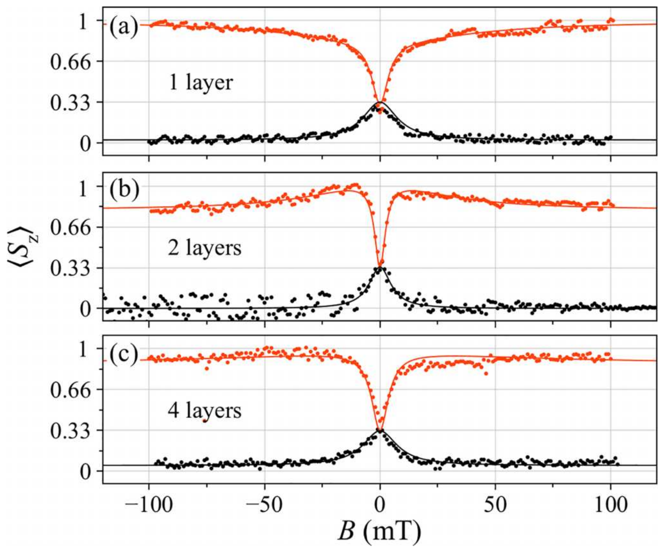

FIG. 4. Polarization recovery curves (red) and Hanle effect measurements (black) for (a) single-layer sample, (b) two-layer sample, and (c) four-layer sample. The measurements show the total spin polarization $\langle S_z \rangle$ as a function of magnetic field strength. The fits for PRCs are done with Eq. (5). The pump power is 20 mW and probe power is 2 mW for both PRCs and Hanle, for single- and two-layer samples, and the pump power for the four-layer sample is 10 mW. All measurements are performed at 6 K.

g-factors between one- and two-layer samples. However, the four-layer sample shows a significant decrease in g-factors. This is related to the differences in excitation energy between the samples. It is demonstrated that with increasing excitation energy, the electron g-factor decreases [16,20]. In our case, the excitation energy is significantly increased in the four-layer sample, leading to a decreased electron g-factor. The same applies to the eight-layer sample in Ref. [7], where the g-factors are $|g_e| = 1.88$ and $|g_h| = 0.60$. The electron g-factor is significantly larger, which is expected, since the excitation done is at lower energies due to a redshift of the sample PL.

Figures 4(a)–4(c) show polarization recovery curves (PRCs) and Hanle measurements for the single-, two-, and four-layer samples, respectively. Both Hanle (black data points and curve) and PRC (red data points and curve) measurements are performed by measuring Faraday ellipticity immediately before pump and probe overlap, ensuring sufficient spin decay and measurements of the resident carriers. The main difference is that Hanle is measured in Voigt geometry, while PRC in Faraday geometry.

As mentioned in the Sec. II, our sample is doped to provide electrons as resident carriers. It has been demonstrated previously that PRCs exhibit a V-like shape for n-doped samples and an M-shape for p-doped samples [21]. From the single-layer sample PRC demonstrated in Fig. 4(a), it can be seen that there are both electrons and holes as the resident carriers. However, in the two- and four-layer samples [Fig. 4(b)], a more prominent M shape is observed, indicating that the electrons are observed as part of trions and holes are becoming resident carriers, showing that by adding additional layers, the number of holes as resident carriers increases. This can be attributed to electrons tunneling out to occupy lower-energy QDs, due to their lower effective mass [7,22], leading to optically induced hole doping.

The fits for both PRC and Hanle are done with Lorentzians that are provided by Ref. [8]:

$$H(\Omega_L) \approx \frac{2}{3}\frac{\delta^2}{2\delta^2 + \Omega_L^2}, \tag{4}$$

$$P(\Omega_L) \approx \frac{1}{3}\frac{2\delta^2 + 3\Omega_L^2}{2\delta^2 + \Omega_L^2}, \tag{5}$$

where P denotes PRC, H denotes the Hanle curve, δ denotes dispersion of the nuclear fluctuations, and $\Omega_L = g\mu_B B/\hbar$. This model is applied by first fitting the Hanle curve with the known transverse g-factor to obtain the dispersion δ, which is then used to fit the PRC's dispersion value and the carrier longitudinal g-factor. This basic model assumes that the hyperfine interaction is isotropic and that nuclear spin precession is significantly slower than electron spin precession. It should be noted that, due to the use of pulsed excitation, we are plotting total spin polarization rather than normalized spin polarization. In such a case, the fit is $\langle S_z \rangle = S_0 P(\Omega_L)$, where S_0 is the initial spin polarization [8]. The reason for this is explained in Ref. [8], Sec V. In the single-layer sample, the PRC fitting yields electron dispersion values of $\delta_e = 2870 \pm 100\ \mu\text{s}^{-1}$ and hole dispersion values of $\delta_h = 360 \pm 10\ \mu\text{s}^{-1}$. For the two-layer sample, the electron dispersion slightly increases to $\delta_e = 3180 \pm 100\ \mu\text{s}^{-1}$ and the obtained hole dispersion is $\delta_h = 261 \pm 10\ \mu\text{s}^{-1}$. As for the four-layer sample, the dispersion values remain similar, $\delta_e = 3200 \pm 400\ \mu\text{s}^{-1}$ and $\delta_h = 326 \pm 10\ \mu\text{s}^{-1}$. These widths indicate how strong the hyperfine interaction is [8], which means that for holes, the hyperfine interaction is significantly lower, which is expected since the nuclear interaction hyperfine constant of a hole is an order of magnitude smaller than for the electron [23]. Moreover, an offset is seen in the Hanle curve of the four-layer sample. This indicates that spin mode-locking is present, which we confirm and discuss in the text below.

Returning to the aforementioned exponential decay component present in the four-layer sample and shown in Fig. 1(e), Figs. 5(a) and 5(b) prove that the additional component is not related to Faraday geometry. Figure 5(a) shows the change of amplitude of the Faraday ellipticity signal, and Fig. 5(b) shows the change of the decay time of the nonoscillating component as the sample is rotated. It can be seen that no matter the rotation angle, the nonoscillating exponential component remained present. It should be noted that, although the lowest decay time would be expected at a 0° angle due to the magnetic field being entirely in Voigt geometry, mechanical rotation of the sample introduces inaccuracies in determining the magnetic field angle.

Additionally, Fig. 5(c) shows the temperature dependence of the exponential decay time (red curve corresponds to the exponential fit). In a magnetic field applied in the Faraday geometry, one would expect the measurement to reflect spin lifetime T_1, which typically decreases with increasing temperature [6,7,24]. Instead, the decay time in our case remains nearly constant up to 50 K, after which it increases exponentially. A similar trend was reported in Ref. [25], where exciton lifetimes were measured in QD molecules using time-resolved microphotoluminescence. These observations

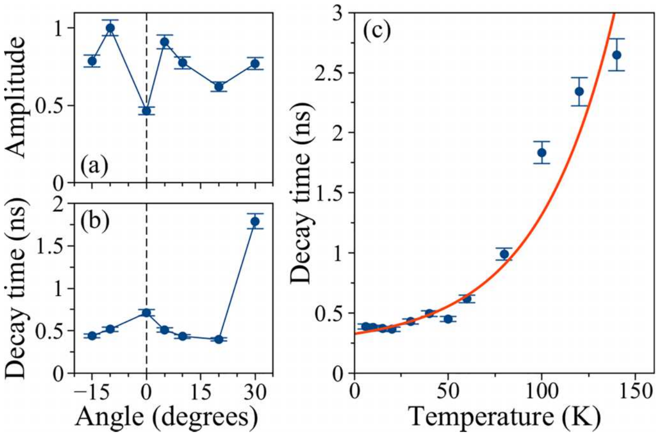

FIG. 5. Characterization of the additional exponential decay component observed in a four-layer QD sample. (a) Normalized amplitude of the exponential component as a function of magnetic field angle measured away from the Voigt geometry. (b) Decay time of the exponential component as a function of magnetic field angle. (c) Temperature dependence of the exponential component decay time. All measurements are performed at a temperature of 6 K [except for (c)], a transverse magnetic field strength of 0.4 T, a pump power of 10 mW, and a probe power of 2 mW.

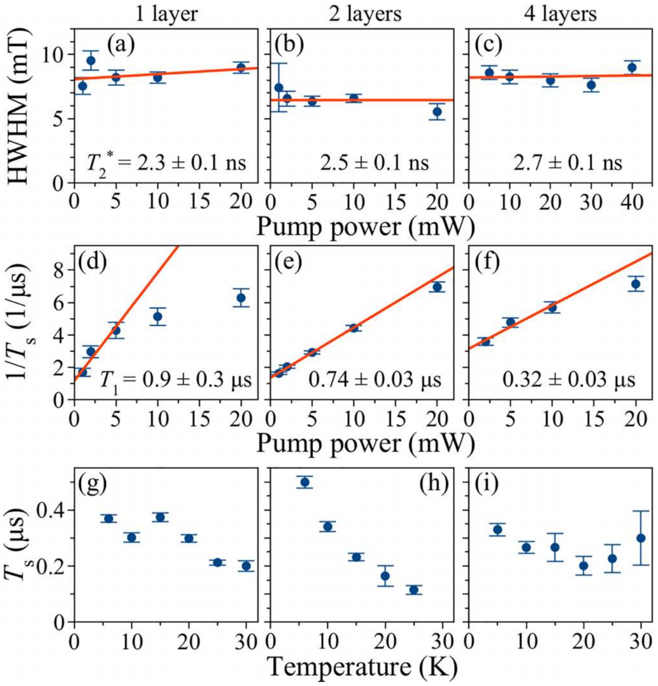

FIG. 6. Spin dynamics measurements for QD samples with different numbers of layers (one, two, and four layers). Panels (a), (b), and (c) display the half-width at half-maximum (HWHM) of Hanle curves as a function of pump power, from which spin dephasing times T_2^* are extracted through linear extrapolation to zero pump power. Panels (d), (e), and (f) show the inverse spin lifetime ($1/T_s$) vs pump power measured under a longitudinal magnetic field of 0.1 T, with the intrinsic longitudinal spin relaxation times T_1 determined by extrapolating the linear fits to zero pump power. Red lines are linear fits for extrapolation to zero. Panels (g), (h), and (i) show the spin lifetime in Faraday geometry dependency on the sample temperature, measured using the spin inertia method. All the samples are subjected to a magnetic field of 0.1 T. Pump power for the different panels is (g) 5 mW, (h) 2 mW, and (i) 2 mW. Measurements in panels (a)–(f) were performed at 6 K and a probe power of 2 mW.

support the conclusion that the exponential decay component originates when additional QD layers are added. However, this is not necessarily related to interdot coupling effects. This is further addressed in the IV.

Figure 6 presents the different spin relaxation times for our samples. In Figs. 6(a)–6(c), Hanle measurements are performed at varying pump powers to extract the HWHM, from which the intrinsic spin dephasing time is determined by extrapolating to zero pump power using the following equation:

$$T_2^* = \frac{\hbar}{g\mu_B B_{\mathrm{HWHM}}}. \tag{6}$$

The extrapolation to zero is done using a linear fit [red curve in Figs. 6(a)–6(c)]. The resulting spin dephasing times can be seen in Table II, showing only slight increase between the different samples. However, the obtained dephasing times are lower than the theoretical limit imposed by hyperfine interaction. To evaluate this limit, the hyperfine interaction strength can be calculated by fitting the PRC curves of all the samples with the following equation [26]:

$$\bar{S}_z = S_0\left[\frac{1}{3} + \frac{2}{3}\frac{B_{\mathrm{ext}}^2}{B_{\mathrm{ext}}^2 + B_f^2}\right], \tag{7}$$

where B_{ext} is the applied magnetic field, S_0 is the average electron-spin polarization at zero magnetic field, and B_f is the averaged nuclear fluctuation field strength, which is the half-width at half-minimum (HWHM) of the PRC dip. This equation is used to fit two components of the PRC, since we observe both a hole and an electron component in all samples. The results of the fits for the hole component of the single-layer sample are $B_f = 5.2$ and 2.4 mT for the two-layer sample, and $B_f = 3.9$ mT for the four-layer sample. With this, the spin dephasing time limited by hyperfine interaction for holes can be calculated with the following equation [27]:

$$T_2^* = 2\sqrt{3}\hbar/(g_h\mu_B B_f), \tag{8}$$

which results in 12 ns for the single-layer sample, 23 ns for the two-layer one, and 20 ns for the four-layer sample. The T_2^*

TABLE II. Spin dephasing times (T_2^*) and longitudinal spin relaxation times (T_1) measured for hole spin carriers across the different QD layer structures. The T_2^* value was not measured by Hanle in Ref. [7].

Sample type	$T_{2,h}^*$ (ns)	$T_{1,h}$ (μs)
Single-layer	2.3 ± 0.1	0.9 ± 0.3
Two-layer	2.5 ± 0.1	0.74 ± 0.03
Four-layer	2.7 ± 0.1	0.32 ± 0.03
Eight-layer [7]		0.50 ± 0.04

values obtained from Hanle measurements are significantly lower, indicating that effects beyond the hyperfine interaction further reduce the dephasing times. One possibility is strain-induced effects that give rise to nuclear quadrupolar interactions, which can significantly reduce spin coherence times [28]. The inherent lattice mismatch in InAs/InAlGaAs QDs grown by SK creates structural asymmetries that enhance these quadrupolar effects. This interpretation is supported by recent studies on InAs/InGaAs/InP QDs grown by metalorganic vapor-phase epitaxy (MOVPE) droplet epitaxy, which demonstrate substantially improved spin dephasing times approaching the hyperfine limit due to the reduced strain achieved through this growth technique [24]. It should be noted that these equations are usually applied for electrons rather than holes. Holes demonstrate significantly weaker hyperfine interactions compared to electrons [23], so this is only an approximation; however, such spin dephasing times are expected for holes [29].

Figures 6(d)–6(f) show T_1 measurements obtained using the spin inertia method [30]. In this measurement approach, a longitudinal magnetic field decouples carrier spins from nuclear spin fluctuations. With the probe delay fixed at a negative time, the pump modulation frequency is varied while monitoring the Faraday ellipticity signal. As the modulation period approaches the spin lifetime, the measured spin polarization diminishes, reducing the average signal amplitude according to the relation [7]

$$S(f_m) = \frac{S_0}{\sqrt{1 + (2\pi f_m T_s)^2}}, \tag{9}$$

where S_0 is the initial amplitude of the Faraday ellipticity signal and f_m is the pump beam polarization EOM modulation frequency. By measuring T_s at different pump powers with a longitudinal magnetic field applied, a linear fit can be applied [red curve in Figs. 6(d)–6(f)].

The intrinsic longitudinal spin relaxation time T_1 is extracted from the measured spin-inertia lifetime T_S using the rate equation [30]

$$\frac{1}{T_s} = \frac{1}{T_1} + \frac{G}{n_0}, \tag{10}$$

where n_0 represents the resident carrier concentration and G is the rate of optical carrier generation. The second term describes the loss of macroscopic spin polarization due to the recombination of resident carriers with photogenerated carriers of the opposite charge. At low excitation densities, G is directly proportional to the incident pump power, leading to a linear increase in the measured relaxation rate $1/T_S$. The intrinsic time T_1 is determined by extrapolating this linear dependence to zero power ($G \to 0$). At higher pump powers, we observe a deviation from linearity, with $1/T_S$ saturating. We attribute this behavior to absorption bleaching (state filling) of the quantum dot ground states. In this regime, the generation rate G saturates due to Pauli blocking, causing the pump-induced decay rate to become independent of the excitation power.

The T_1 values across the samples can be seen in Table II.

The difference in T_1 times between single- and two-layer samples is significant, but the error in the single-layer sample T_1 is large enough to put it within the range of the two-layer sample. However, the four-layer sample shows a further reduction compared to both the single- and two-layer samples. The eight-layer sample in Ref. [7] also exhibits a reduced T_1 of 0.5 μs, indicating that the shift from two- to four-layers causes a reduction in T_1 times. Figure 4 demonstrates that with added layers, the effective carriers become holes; therefore, it is also safe to assume that the T_1 measurements are for holes when additional layers are added. This transition to hole-dominated charging contributes to the observed reduction in T_1 times, as holes exhibit enhanced spin-orbit coupling compared to electrons, which accelerates spin relaxation processes [31,32]. Moreover, the hole spin lifetime also shows a strong dependence on QD size. It was demonstrated that larger InAs/GaAs dots exhibit longer T_1 times [33]. The particularly low T_1 observed in the four-layer sample can be understood through the interplay of these effects: the resident carriers are holes, which have an inherently shorter lifetime, and the sample was excited at a higher energy compared to the single- and two-layer samples, which excite smaller QDs within the ensemble, leading to shorter T_1 times for holes. In contrast, the eight-layer sample in Ref. [7] was excited at a lower energy, corresponding to larger QDs with longer T_1 times. However, this value remains lower than those of single- and two-layer samples because holes are the dominant carriers.

Figures 6(g)–6(i) show the spin lifetime dependence on temperature with a magnetic field applied in Faraday geometry for single-, two-, and four-layer samples, respectively. The spin lifetime values in Fig. 6(i) are significantly lower because of using higher pump power, where it is known that increasing pump power speeds up spin relaxation due to photogenerated carriers, causing delocalization of resident carriers [34]. Another factor is the intrinsically lower T_1 time for the four-layer structure, shown in Fig. 6(f). The measurements were done up to 25–30 K because the signal weakened as the temperature increased, making the fitting error too large at higher temperatures. The changing trend across different layer count structures is further addressed in the IV.

Lastly, in Fig. 7(a), the signal of the four-layer sample and its fit (red curve) are displayed. In this case, a weak, single-frequency oscillation can be observed [see Fig. 7(c) and zoom-in]. This effect is called spin mode-locking (SML). In SML, coherent spin dynamics are sustained across multiple pump-pulse cycles via a feedback mechanism. When the spin coherence time T_2 exceeds the laser repetition period T_R, spins that precess commensurate with the pulse repetition frequency can maintain phase coherence between successive excitation pulses [7,35]. This manifests as a revival of the spin signal at negative time delays, where the probe pulse arrives before the pump pulse. In this case, the SML signal frequency corresponds to holes, since the SML signal frequency is the same as the hole precession frequency seen at positive time delays.

The existence of SML allows us to estimate T_2 for the four-layer sample. The hole spin coherence time T_2 was extracted by modeling the SML signal amplitude ratio before and after pump pulse excitation. The modeling incorporated experimentally determined hole g-factors, g-factor spreads (Δg_h), and assumed a Gaussian distribution of g-factors across the QD ensemble. References [7,13,35,36] go into more details about how the modeling is done.

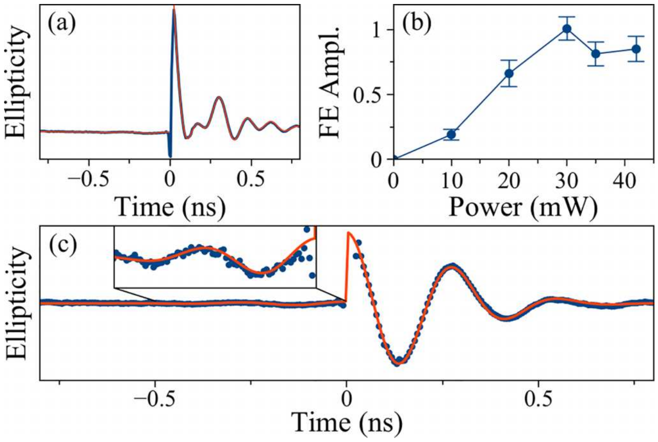

FIG. 7. (a) Time-resolved pump-probe signal for the four-layer sample, where the blue trace represents the raw data and the red line is a fit. At negative time delays (on the left), the signal shows the characteristic SML revival, in which spin coherence is recovered before the arrival of the pump pulse. At positive time delays (right side), normal spin precession is observed in Voigt geometry following optical excitation. (b) Normalized amplitude of the SML signal as a function of pump power, showing how the mode-locking effect strengthens with increasing excitation power until reaching saturation around 25–30 mW. (c) The extracted SML data for holes (blue data points) fitted with a theoretical model curve (red line). All measurements were performed at 6 K, 0.4 T transverse magnetic field, and 2 mW probe power.

In Ref. [7], the authors were only able to estimate the range of T_2 times due to not observing SML amplitude saturation or Rabi oscillations. In our case, we can determine it much more accurately by observing saturation of the SML amplitude, as shown in Fig. 7(b). To determine it, we model the QD ensemble using a Gaussian g-factor distribution with a width of $\Delta g_h = 0.11$ and g-factor $|g_h| = 0.65$. The amplitude ratio of SML and the amplitude of the signal after excitation then depends on T_2 time and the pulse area Θ. Since we observe saturation, the pulse area is $\Theta = \pi$, and thus the coherence time is $T_2 = 13$ ns. The plotted model (red curve corresponds to the model fit) can be seen in Fig. 7(c) overlayed with the extracted hole spin contribution of the real signal given in Fig. 7(a).

IV. DISCUSSION

Several noteworthy effects emerge when additional QD layers with narrow barrier separations are incorporated. First, the n-doped sample becomes effectively p-doped when a second layer is added, and with four layers, there is indication that there is again more electron carriers, which is possible due to variances in doping between samples. However, holes are still present, as shown in Figs. 4(a)–4(c). In the previous section, we mentioned that the cause of this is the tunneling of excited electrons to lower-energy QDs. The reason is likely that, as additional layers grow, the QDs on that layer have lower energy. This has been demonstrated for InAs/GaAs QDs, where as layers are stacked, the QD size increases since the strain distribution from the underlying layers causes the preferential localization of QDs on top [37,38]. Moreover, although the barrier thickness is 15 nm, it is not measured from the top of the QDs. The QD height is estimated to be between 9 and 13 nm [19], which makes the effective distance between the QDs short enough (3–6 nm) for tunneling to occur efficiently.

These samples would benefit from added charge-control structures not only because of being able to confidently determine whether the seen changes in doping are truly related to tunneling, but also for extending carrier lifetimes and enabling controlled tuning of tunneling. However, implementing charge control in multilayer structures is challenging because doping can only be applied above and below the QD layer stack. Due to this, deterministic charging of each layer is hard to achieve due to the lack of uniformity of the electric field and the Fermi level.

In addition to tunneling, we see an additional nonoscillating decaying exponential starting to appear in the four-layer structure, seen in Fig. 1(d), which is also seen in the eight-layer structure in Ref. [7], Fig. 2(a). In the referenced paper, the authors attribute this additional component to either a molecular or an excitonic state caused by coupling between the QDs. In our case, we also attribute it to coupling-related effects, since we exclude the possibility of the exponential resulting from Faraday geometry by performing anisotropy measurements shown in Figs. 5(a) and 5(b), and also because we do not see the additional component in either single- or two-layer samples.

We hypothesize that there are two effects associated with this nonoscillating component. It is known that, due to QD confinement, there is significant light-hole (LH) and heavy-hole (HH) mixing [39], which affects the optical and spin properties of QDs, in particular, causing significant g-factor anisotropy and nonzero in-plane g-factor values for the corresponding hole component [17]. However, for some quantum-well samples, a pure HH state has been observed, which shows transverse g-factor values near zero [40] or even effectively zero when considering thin quantum wells, in which case the splitting between the LH and HH is relatively large when ignoring cubic symmetry [41]. Therefore, we attribute the nonoscillating component to reduced heavy-hole–light-hole mixing, caused by the addition of multiple layers that change the strain environment and, in turn, reduce symmetry, resulting in greater splitting between LH and HH. This is further confirmed by examining the eight-layer structure in Ref. [7], where the nonoscillating component exhibits an increase in both decay time and amplitude, suggesting that additional layers may further reduce HH and LH mixing.

Subsequently, Fig. 5(c) demonstrates an unexpected result where both the electron and the potential HH dephasing times increase with temperature. These results show substantial similarity to time-resolved microphotoluminescence exciton lifetime measurements in InAs/InP QDs [25] and in InAs/GaAs QDs [42–44], where the lifetime increases with temperature due to the carriers being excited to p-shell states with increased temperature, causing lowered radiative rates since the carriers have to relax back to s-shell before recombining. Moreover, indirect excitons in coupled QD systems have been demonstrated via photoluminescence measurements, using an electric field to place the electron and hole in resonance [45]. Therefore, as we have confirmed that tunneling in our sample is a possibility due to the effective distances between the QDs and due to the results shown in Fig. 4, we then assume that the increasing dephasing times of excitons and heavy-holes seen in Fig. 5(c) are due to the formation of an indirect exciton.

In our case, we do not need to perform electric-field tuning because our measurements show spin polarization rather than photoluminescence. However, the previously discussed measurements in Refs. [25,42–44] show increased exciton lifetime, rather than investigating spin dephasing. The observed dephasing pattern arises because holes in indirect excitons experience primarily hyperfine interactions as their dominant dephasing mechanism [46]. This hyperfine-interaction-limited dephasing directly correlates the hole spin dephasing time with the exciton lifetime. Therefore, as temperature increases, exciton lifetimes increase, and the dephasing time increases proportionally. As to why this is not observed for the direct excitons in either the four-layer or lower count layer samples, this is due to the indirect excitons having an inherently longer lifetime because of their reduced wave-function overlap [47], making them more affected by the aforementioned radiative overlap.

Another emerging effect arising from multiple layers of QDs is evident in Figs. 6(g)–6(i). In Figs. 6(g) and 6(h), the tendencies are expected, where in panel (g), a more or less constant spin lifetime is observed up to 20 K and then starts reducing, which indicates that the resident carriers are electrons [6]. In plot (h), the lifetime starts to decrease immediately at 10 K, suggesting that the resident carriers are then holes [6]. The PRC results in Figs. 4(a) and 4(b) further confirm these two plots. In the case of Fig. 6(i), it is expected that it would be the same as in plot (h), due to the resident carriers being holes; however, the spin lifetime remains nearly constant through the whole range. Almost identical behavior is observed in the eight-layer sample investigated in Ref. [7], indicating that this effect, like SML and the nonoscillating component, only appears at four layers or more.

Lastly, along with the additional component observed in the four-layer sample, we also observe spin mode-locking. Moreover, we can see improvements in T_2 times from a four-layer sample to an eight-layer sample, as shown in Ref. [7]; however, these are relatively marginal and, in this case, are attributed to error. As to the reason for SML's appearance, it can be explained by the aforementioned tunneling. As more and more layers are added, there are more QDs for electrons to tunnel to, leaving more holes behind. This greatly increases the hole population, which allows us to observe SML. As for the T_2 values themselves, they are relatively low compared to $T_2 = 1.1\,\mu\text{s}$ of AlAs/GaAs QDs [48]. However, hole-spin coherence times have not been reported previously in telecom QDs. Therefore, this shows that multilayer QD structures have potential for quantum information applications. To gain better insight not only into T_2 but also into other phenomena we have observed in this paper, additional measurements and analyses are needed.

V. CONCLUSIONS

This layer-resolved study identifies how vertical stacking of MBE-grown telecom C-band QDs impacts spin properties, revealing several phenomena that emerge with increasing layer count in InAs/InAlGaAs QD configurations. The transition from electron-dominated to hole-dominated resident carriers with increasing layers represents a fundamental shift in spin dynamics: single-layer samples exhibit both electron and hole components, whereas two- and four-layer samples show predominantly holelike behavior due to electron tunneling to lower-energy dots in additional layers. Four-layer structures exhibit distinctive interlayer coupling effects, including an additional nonoscillatory exponential-decay component that persists across all magnetic field angles, with an unusual temperature dependence in which spin relaxation times increase rather than decrease with temperature, attributed to indirect exciton effects. Also, spin mode locking emerges that enables direct measurement of hole coherence times $T_2 \approx 13$ ns. While transverse dephasing times T_2^* remain relatively stable across layer counts (2.3–2.7 ns), they fall short of hyperfine-limited theoretical values, suggesting additional dephasing mechanisms such as strain-induced quadrupolar interactions. The reduction in longitudinal relaxation time T_1 with increasing layers (from 0.9 to 0.3 μs) highlights the tradeoff between optical signal enhancement and spin-lifetime preservation.

Across all layer numbers studied, the results show that the relevant spin properties, carrier type, and coherence behavior do not degrade (except T_1) with increasing layer count. Instead, multilayer stacks support hole spins with stable coherence characteristics, indicating that vertical coupling can be used as a design parameter rather than a limitation. These findings demonstrate that multilayer telecom QDs remain a viable platform for spin-photon schemes and guide engineering stacked structures where hole-spin coherence is the operative resource.

ACKNOWLEDGMENTS

We thank N. E. Kopteva for valuable discussions and help with the SML model. We acknowledge financial support from the Bundesministerium für Forschung, Technologie und Raumfahrt (BMFTR) within the framework of the joint project QR.N in Dortmund and Kassel (Contracts No. 16KIS2201 and No. 16KIS2204). We also acknowledge financial support from the Deutsche Forschungsgemeinschaft (DFG) through the Heisenberg grant (BE 5778/4-1) and EPSRC Grant No. EP/S030751/1.

DATA AVAILABILITY

The data that support the findings of this article are not publicly available. The data are available from the authors upon reasonable request.

---

[1] D. A. Vajner, L. Rickert, T. Gao, K. Kaymazlar, and T. Heindel, Quantum communication using semiconductor quantum dots, Adv. Quantum Technol. **5**, 2100116 (2022).

[2] T. Miyazawa, K. Takemoto, Y. Nambu, S. Miki, T. Yamashita, H. Terai, M. Fujiwara, M. Sasaki, Y. Sakuma, M. Takatsu, T. Yamamoto, and Y. Arakawa, Single-photon emission at 1.5 μm

from an InAs/InP quantum dot with highly suppressed multiphoton emission probabilities, Appl. Phys. Lett. **109**, 132106 (2016).

[3] P. Holewa, A. Sakanas, U. M. Gur, P. Mrowi'nski, A. Huck, B.-Y. Wang, A. Musiał, K. Yvind, N. Gregersen, M. Syperek, and E. Semenova, Bright quantum dot single-photon emitters at telecom bands heterogeneously integrated on Si, ACS Photon. **9**, 2273 (2022).

[4] S. Bauer, D. Wang, N. Hoppe, C. Nawrath, J. Fischer, N. Witz, M. Kaschel, C. Schweikert, M. Jetter, S. L. Portalupi, M. Berroth, and P. Michler, Achieving stable fiber coupling of quantum dot telecom C-band single-photons to an SOI photonic device, Appl. Phys. Lett. **119**, 211101 (2021).

[5] M. H. Rahaman, S. Harper, C.-M. Lee, K.-Y. Kim, M. Buyukkaya, V. Patel, S. Hawkins, J.-H. Kim, S. Addamane, and E. Waks, Efficient, indistinguishable telecom C-band photons using a tapered nanobeam waveguide, ACS Photon. **11**, 2738 (2024).

[6] A. V. Mikhailov, V. V. Belykh, D. R. Yakovlev, P. S. Grigoryev, J. P. Reithmaier, M. Benyoucef, and M. Bayer, Electron and hole spin relaxation in InP-based self-assembled quantum dots emitting at telecom wavelengths, Phys. Rev. B **98**, 205306 (2018).

[7] E. Evers, N. E. Kopteva, V. Nedelea, A. Kors, R. Kaur, J. P. Reithmaier, M. Benyoucef, M. Bayer, and A. Greilich, Hole spin coherence in InAs/InAlGaAs self-assembled quantum dots emitting at telecom wavelengths, Phys. Status Solidi B **262**, 2400174 (2025).

[8] D. S. Smirnov, E. A. Zhukov, D. R. Yakovlev, E. Kirstein, M. Bayer, and A. Greilich, Spin polarization recovery and Hanle effect for charge carriers interacting with nuclear spins in semiconductors, Phys. Rev. B **102**, 235413 (2020).

[9] X. Li, Q. Xu, and Z. Zhang, Molecular beam epitaxy growth of quantum wires and quantum dots, Nanomaterials **13**, 960 (2023).

[10] E. A. Stinaff, M. Scheibner, A. S. Bracker, I. V. Ponomarev, V. L. Korenev, M. E. Ware, M. F. Doty, T. L. Reinecke, and D. Gammon, Optical signatures of coupled quantum dots, Science **311**, 636 (2006).

[11] D. Kim, S. E. Economou, C. C. Bădescu, M. Scheibner, A. S. Bracker, M. Bashkansky, T. L. Reinecke, and D. Gammon, Optical spin initialization and non-destructive measurement in a quantum dot molecule, Phys. Rev. Lett. **101**, 236804 (2008).

[12] D. Wigger, J. Schall, M. Deconinck, N. Bart, P. Mrowiński, M. Krzykowski, K. Gawarecki, M. von Helversen, R. Schmidt, L. Bremer, F. Bopp, D. Reuter, A. D. Wieck, S. Rodt, J. Renard, G. Nogues, A. Ludwig, P. Machnikowski, J. J. Finley, S. Reitzenstein, *et al.*, Controlled coherent coupling in a quantum dot molecule revealed by ultrafast four-wave mixing spectroscopy, ACS Photon. **10**, 1504 (2023).

[13] I. A. Yugova, M. M. Glazov, E. L. Ivchenko, and A. L. Efros, Pump-probe Faraday rotation and ellipticity in an ensemble of singly charged quantum dots, Phys. Rev. B **80**, 104436 (2009).

[14] J. H. Prechtel, F. Maier, J. Houel, A. V. Kuhlmann, A. Ludwig, A. D. Wieck, D. Loss, and R. J. Warburton, Electrically tunable hole g factor of an optically active quantum dot for fast spin rotations, Phys. Rev. B **91**, 165304 (2015).

[15] L. Sapienza, R. M. Al-Khuzheyri, A. C. Dada, A. Griffiths, E. Clarke, and B. D. Gerardot, Magneto-optical spectroscopy of single charge-tunable InAs/GaAs quantum dots emitting at telecom wavelengths, Phys. Rev. B **93**, 155301 (2016).

[16] V. V. Belykh, A. Greilich, D. R. Yakovlev, M. Yacob, J. P. Reithmaier, M. Benyoucef, and M. Bayer, Electron and hole g factors in InAs/InAlGaAs self-assembled quantum dots emitting at telecom wavelengths, Phys. Rev. B **92**, 165307 (2015).

[17] V. V. Belykh, D. R. Yakovlev, J. J. Schindler, E. A. Zhukov, M. A. Semina, M. Yacob, J. P. Reithmaier, M. Benyoucef, and M. Bayer, Large anisotropy of electron and hole g factors in infrared-emitting InAs/InAlGaAs self-assembled quantum dots, Phys. Rev. B **93**, 125302 (2016).

[18] L. M. Roth, B. Lax, and S. Zwerdling, Theory of optical magneto-absorption effects in semiconductors, Phys. Rev. **114**, 90 (1959).

[19] V. V. Belykh, D. R. Yakovlev, J. J. Schindler, J. van Bree, P. M. Koenraad, N. S. Averkiev, M. Bayer, and A. Y. Silov, Dispersion of the electron g factor anisotropy in InAs/InP self-assembled quantum dots, J. Appl. Phys. **120**, 084301 (2016).

[20] D. Kim, W. Sheng, P. J. Poole, D. Dalacu, J. Lefebvre, J. Lapointe, M. E. Reimer, G. C. Aers, and R. L. Williams, Tuning the exciton g factor in single InAs/InP quantum dots, Phys. Rev. B **79**, 045310 (2009).

[21] E. A. Zhukov, E. Kirstein, D. S. Smirnov, D. R. Yakovlev, M. M. Glazov, D. Reuter, A. D. Wieck, M. Bayer, and A. Greilich, Spin inertia of resident and photoexcited carriers in singly charged quantum dots, Phys. Rev. B **98**, 121304(R) (2018).

[22] I. Mikhailov, L. García, and J. Marín, Vertically coupled quantum dots charged by exciton, Microelectron. J. **39**, 378 (2008), The Sixth International Conference on Low Dimensional Structures and Devices.

[23] C. Testelin, F. Bernardot, B. Eble, and M. Chamarro, Hole–spin dephasing time associated with hyperfine interaction in quantum dots, Phys. Rev. B **79**, 195440 (2009).

[24] M. Cizauskas, E. M. Sala, J. Heffernan, A. M. Fox, M. Bayer, and A. Greilich, Spin properties in droplet epitaxy-grown telecom quantum dots, Phys. Rev. B **112**, 165412 (2025).

[25] R. Hostein, A. Michon, G. Beaudoin, N. Gogneau, G. Patriache, J.-Y. Marzin, I. Robert-Philip, I. Sagnes, and A. Beveratos, Time-resolved characterization of InAsP/InP quantum dots emitting in the C-band telecommunication window, Appl. Phys. Lett. **93**, 073106 (2008).

[26] M. Y. Petrov, I. V. Ignatiev, S. V. Poltavtsev, A. Greilich, A. Bauschulte, D. R. Yakovlev, and M. Bayer, Effect of thermal annealing on the hyperfine interaction in InAs/GaAs quantum dots, Phys. Rev. B **78**, 045315 (2008).

[27] A. Greilich, A. Pawlis, F. Liu, O. A. Yugov, D. R. Yakovlev, K. Lischka, Y. Yamamoto, and M. Bayer, Spin dephasing of fluorine-bound electrons in ZnSe, Phys. Rev. B **85**, 121303(R) (2012).

[28] R. Stockill, C. Le Gall, C. Matthiesen, L. Huthmacher, E. Clarke, M. Hugues, and M. Atatüre, Quantum dot spin coherence governed by a strained nuclear environment, Nat. Commun. **7**, 12745 (2016).

[29] T. M. Godden, J. H. Quilter, A. J. Ramsay, Y. Wu, P. Brereton, S. J. Boyle, I. J. Luxmoore, J. Puebla Nunez, A. M. Fox, and M. S. Skolnick, Coherent optical control of the spin of a single hole in an InAs/GaAs quantum dot, Phys. Rev. Lett. **108**, 017402 (2012).

[30] F. Heisterkamp, E. A. Zhukov, A. Greilich, D. R. Yakovlev, V. L. Korenev, A. Pawlis, and M. Bayer, Longitudinal and transverse spin dynamics of donor-bound electrons in fluorine-doped ZnSe: Spin inertia versus Hanle effect, Phys. Rev. B **91**, 235432 (2015).

[31] D. V. Bulaev and D. Loss, Spin relaxation and decoherence of holes in quantum dots, Phys. Rev. Lett. **95**, 076805 (2005).

[32] L. Chirolli and G. Burkard, Decoherence in solid-state qubits, Adv. Phys. **57**, 225 (2008).

[33] H. Wei, M. Gong, G. Guo, and L. He, Atomistic pseudopotential theory of spin relaxation in self-assembled $\mathrm{In}_{1-x}\mathrm{Ga}_x\mathrm{As}$/GaAs quantum dots at zero magnetic field, Phys. Rev. B **85**, 045317 (2012).

[34] E. A. Zhukov, D. R. Yakovlev, M. Bayer, M. M. Glazov, E. L. Ivchenko, G. Karczewski, T. Wojtowicz, and J. Kossut, Spin coherence of a two-dimensional electron gas induced by resonant excitation of trions and excitons in CdTe/(Cd,Mg)Te quantum wells, Phys. Rev. B **76**, 205310 (2007).

[35] A. Greilich, D. R. Yakovlev, A. Shabaev, A. L. Efros, I. A. Yugova, R. Oulton, V. Stavarache, D. Reuter, A. Wieck, and M. Bayer, Mode locking of electron spin coherences in singly charged quantum dots, Science **313**, 341 (2006).

[36] I. A. Yugova, M. M. Glazov, D. R. Yakovlev, A. A. Sokolova, and M. Bayer, Coherent spin dynamics of electrons and holes in semiconductor quantum wells and quantum dots under periodical optical excitation: Resonant spin amplification versus spin mode locking, Phys. Rev. B **85**, 125304 (2012).

[37] H. J. Krenner, S. Stufler, M. Sabathil, E. C. Clark, P. Ester, M. Bichler, G. Abstreiter, J. J. Finley, and A. Zrenner, Recent advances in exciton-based quantum information processing in quantum dot nanostructures, New J. Phys. **7**, 184 (2005).

[38] M. Usman, T. Inoue, Y. Harda, G. Klimeck, and T. Kita, Experimental and atomistic theoretical study of degree of polarization from multilayer InAs/GaAs quantum dot stacks, Phys. Rev. B **84**, 115321 (2011).

[39] J. Luo, G. Bester, and A. Zunger, Supercoupling between heavy-hole and light-hole states in nanostructures, Phys. Rev. B **92**, 165301 (2015).

[40] X. Marie, T. Amand, P. Le Jeune, M. Paillard, P. Renucci, L. E. Golub, V. D. Dymnikov, and E. L. Ivchenko, Hole spin quantum beats in quantum-well structures, Phys. Rev. B **60**, 5811 (1999).

[41] M. A. Semina, A. A. Golovatenko, and A. V. Rodina, Cubic anisotropy of hole Zeeman splitting in semiconductor nanocrystals, Phys. Rev. B **108**, 235310 (2023).

[42] H. Yu, S. Lycett, C. Roberts, and R. Murray, Time resolved study of self-assembled InAs quantum dots, Appl. Phys. Lett. **69**, 4087 (1996).

[43] A. Fiore, P. Borri, W. Langbein, J. M. Hvam, U. Oesterle, R. Houdré, R. P. Stanley, and M. Ilegems, Time-resolved optical characterization of InAs/InGaAs quantum dots emitting at 1.3 μm, Appl. Phys. Lett. **76**, 3430 (2000).

[44] G. Wang, S. Fafard, D. Leonard, J. E. Bowers, J. L. Merz, and P. M. Petroff, Time-resolved optical characterization of InGaAs/GaAs quantum dots, Appl. Phys. Lett. **64**, 2815 (1994).

[45] J. M. Daniels, P. Machnikowski, and T. Kuhn, Excitons in quantum dot molecules: Coulomb coupling, spin-orbit effects, and phonon-induced line broadening, Phys. Rev. B **88**, 205307 (2013).

[46] J. Rautert, T. S. Shamirzaev, S. V. Nekrasov, D. R. Yakovlev, P. Klenovsk'y, Y. G. Kusrayev, and M. Bayer, Optical orientation and alignment of excitons in direct and indirect band gap (In,Al)As/AlAs quantum dots with type-I band alignment, Phys. Rev. B **99**, 195411 (2019).

[47] K. Sivalertporn, L. Mouchliadis, A. L. Ivanov, R. Philp, and E. A. Muljarov, Direct and indirect excitons in semiconductor coupled quantum wells in an applied electric field, Phys. Rev. B **85**, 045207 (2012).

[48] K. D. Greve, P. L. McMahon, D. Press, T. D. Ladd, D. Bisping, C. Schneider, M. Kamp, L. Worschech, S. Hoefling, A. Forchel, and Y. Yamamoto, Ultrafast coherent control and suppressed nuclear feedback of a single quantum dot hole qubit, Nat. Phys. **7**, 872 (2011).